Computation of Self-Similar Solutions for Mean Curvature Flow

David L. Chopp

CONTENTS

We describe a numerical algorithm to compute surfaces that are approximately self-similar under mean curvature flow. The method restricts computation to a two-dimensional subspace of the space of embedded manifolds that is likely to contain a self-similar solution.

Using the algorithm, we recover the self-similar torus of Angenent and find several surfaces that appear to approximate previously unknown self-similar surfaces. Two of them may prove to be counterexamples to the conjecture of uniqueness of the weak solution for mean curvature flow for surfaces.

1. INTRODUCTION

Curves and surfaces that change by a similarity transformation under mean curvature flow have become a focus of attention in the study of this type of flow. Apart from their intrinsic interest, there appears to be a link between singularities in motion by mean curvature and self-similar shapes. This connection is displayed by Grayson's result [1987] that curves in $\mathbb{R}^2$ shrink to round points under motion by curvature. This can be rephrased by saying that every closed embedded curve in $\mathbb{R}^2$ flows toward a self-similar solution as it approaches singularity, and that a circle is the only such self-similar solution.

For two-dimensional manifolds in $\mathbb{R}^3$, the problem is much more difficult and not as well understood. However, recent results indicate that self-similar solutions and singularities are connected here as well. For example, Huisken [1984] showed that convex manifolds shrink to spheres under motion by mean curvature. Grayson [1989] was able to prove that the convexity condition is necessary.

Recently, Angenent [1992] proved the existence of a self-similar torus, then used that torus to give an alternative proof that the convexity condition is necessary. This demonstrates the utility of self-similar solutions in the study of singularities. The best result showing the link between self-similarity and singularity is by Huisken [1991], who proves that if the curvature at a singularity is bounded by $c(T - t)^{-1/2}$, where t is time, T is the time of singularity and c is a constant, then the surface evolves towards a self-similar surface at the point of singularity.

A second theoretical question involves the weak solution for mean curvature flow. It is known that, for self-intersecting plane curves, the weak solution for curvature develops a nonempty interior at the point of self-intersection. But Grayson's result shows that a smooth curve will not self-intersect, and hence not develop an interior.

We may ask the same question about higher-dimensional surfaces flowing by mean curvature. For instance, it is known that a fat torus of revolution develops a singularity in the center of the hole as it evolves towards a sphere, while a skinny torus evolves towards a circle as the cross-sectional area goes to zero (see Section 2.2). It was once conjectured that a torus with an initial ratio on the boundary of these two regimes would develop an interior. However, the discoveries by Angenent and Huisken have shown that this particular torus evolves instead into a self-similar torus. Whether a smooth initial surface can develop an interior remains an open question, but we believe that two examples given below (Sections 4.4 and 4.6) may lead to an affirmative answer.

In related work, some progress on the occurence of singularities and evolution past singularities for surfaces of revolution has been made recently [Altshuler et al. 1993].

Currently, very few examples of two-dimensional embedded self-similar solutions for motion by mean curvature have been proved to exist, all of them being surfaces of revolution. In this paper, we design a numerical algorithm to compute approximations

to other self-similar solutions, and give strong numerical evidence that these are good approximations.

We describe the algorithm in Section 2, including a modified form of the differential equation for motion by mean curvature. In Section 3 we discuss ways of testing the reliability of the results. Section 4 displays several examples of surfaces computed by the algorithm, and Section 5 concludes with a discussion of future research directions.

2. THE ALGORITHM

2.1. Overview

The algorithm we use is based upon the level set method for propagating interfaces introduced by Osher and Sethian [1988]. The numerical methods which led up to the level set method can be found in [Sethian 1985], and for a review of numerical methods for curvature flow see [Sethian 1989]. The theoretical aspects of this method were studied by Evans and Spruck [1991; 1992]. For further theoretical work, see also [Chen et al. 1991; Evans et al. 1992; Falcone et al. 1990; Giga and Goto 1992]. The level set method has been applied to a number of other applications: see, for example, [Chopp 1992; 1993; Chopp and Sethian 1993; Sethian and Strain 1992].

We give a brief overview of the level set method as it applies here. The idea is to represent the evolving two-dimensional manifold as the level set (for each t) of a function φ of $x \in \mathbb{R}^3$ and t. In symbols, the surface at time t is

$$S_\lambda(t) = \{x \in \mathbb{R}^3 : \varphi(x, t) = \lambda\}$$

Motion by mean curvature can now be expressed in terms of φ by

$$\varphi_t(x, t) = H_\varphi(x, t) \, \|\nabla\varphi(x, t)\|,$$

where $H_\varphi(x, t)$ is the mean curvature of the level set $S_{\varphi(x,t)}(t)$ containing x at time t. Notice that this equation does not depend upon the value of the level set: each surface moves according to its own mean curvature. In this way, a whole family

of initial surfaces—the level sets $S_\lambda(0)$—evolves by mean curvature simultaneously. It is this property that is at the heart of our algorithm.

2.2. The Search for Self-Similar Surfaces: An Example

We introduce the method using the problem of finding a self-similar torus. Let M be the space of all compact two-dimensional differentiable manifolds embedded in $\mathbb{R}^3$, modded out by the group of similarity transformations (that is, the group generated by rigid motions and uniform scalings).

Let C be the circle of radius one and center at the origin in the xy-plane, and define $S_\lambda(0)$ as the tube of radius λ around C in $\mathbb{R}^3$. The family $S_\lambda(0)$, for $\lambda \in (0,1)$, is a one-parameter subspace of M. For each λ, let $S_\lambda(t)$ be the result of moving $S_\lambda(0)$ by mean curvature to time t, and define T_λ as the time to singularity for the initial surface $S_\lambda(0)$. The set

$$U = \{(\lambda, t) : \lambda \in (0,1), t \in [0, T_\lambda)\} \subset \mathbb{R}^2$$

parametrizes the subspace of M consisting of surfaces that arise by mean curvature flow from some $S_\lambda(0)$ (Figure 1).
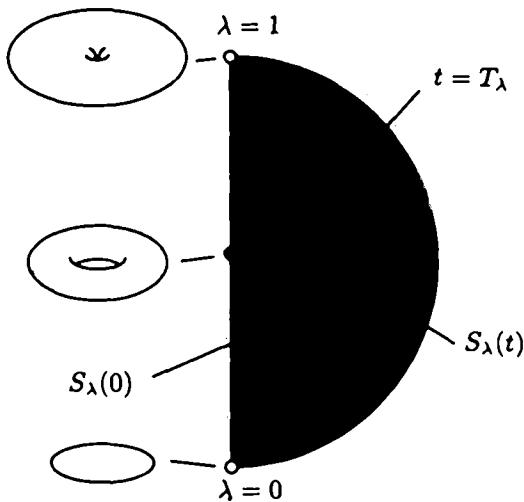

FIGURE 1. In the space M of embedded surfaces modulo similarities, this is the subspace that can be reached by mean curvature flow from the round tori $S_\lambda(0)$.

Next, let $\rho(\lambda, t)$ be the fatness of the torus $S_\lambda(t)$, defined as the ratio of the height in the z-direction

to the radius of the hole (Figure 2). (This definition, of course, depends on the fact that the surface remains symmetric about the z-axis and through the xy-plane). We have $\rho(\lambda, 0) = \lambda/(1 - \lambda)$. For λ
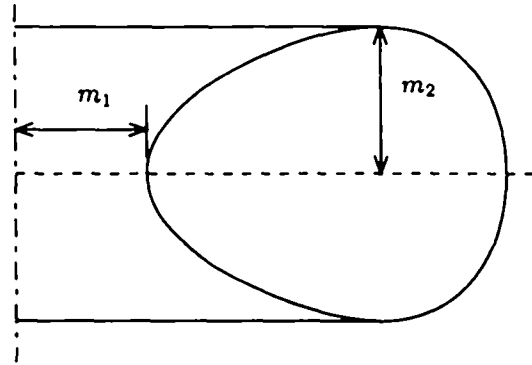

FIGURE 2. By definition, $\rho(\lambda, t)$ is the ratio m_2/m_1 for the torus $\rho(\lambda, t)$.

small, $\rho(\lambda, t)$ starts near zero and decreases with t, approaching 0 as $t \to T_\lambda$: the torus gets ever skinnier, and at time T_λ turns into a circle. Conversely, for λ near one, $\rho(\lambda, t)$ starts large and increases in time, approaching ∞ as $t \to T_\lambda$: the torus gets fatter, and develops a singularity at the center. Thus $\rho(\lambda, t)$ records the way in which a singularity develops.

There is a critical value λ_0 on the boundary of the two regimes: as $t \to T_\lambda$, the ratio $\rho(\lambda, t)$ approaches infinity if $\lambda > \lambda_0$, and approaches zero if $\lambda < \lambda_0$. Because we have continuous initial data, it is reasonable to hope that, for λ critical, $\rho(\lambda_0, t)$ is asymptotically constant, approaching some finite constant $\rho_0 > 0$. Thus, our picture of U including trajectories should look like Figure 3. Our goal, then, is to locate λ_0.

In general, this is hard to do. Regardless of how small $|\lambda - \lambda_0| > 0$ is, $\rho(\lambda, t)$ diverges from $\rho(\lambda_0, t)$ as $t \to T_\lambda$: the system is unstable. Figure 4 illustrates this divergence by showing several trajectories of $\rho(\lambda, t)$ for the tori $S_\lambda(t)$ evolving under mean curvature flow.

Therefore, we must find some other means of locating the trajectory $\rho(\lambda_0, t)$. If the curvature does not blow up too fast, it is reasonable to conclude
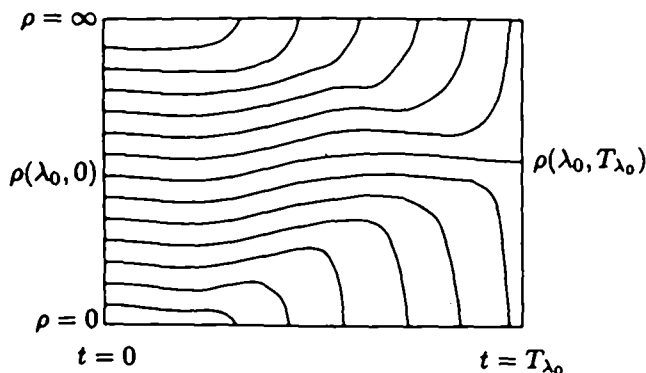
FIGURE 3. Qualitative diagram of the (t, ρ) plane, with the trajectories $\rho(\lambda, t)$ for various λ. The trajectory $\lambda = \lambda_0$ is the only one that tends to a finite (nonzero) value of ρ.
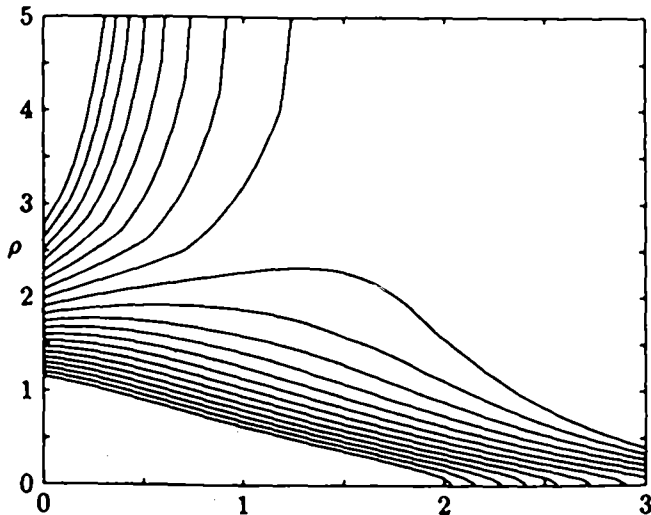

FIGURE 4. Computed trajectories of $S_\lambda(t)$ under mean curvature flow. Each time unit in the horizontal axis represents 10^4 iterations.

that $(\partial \rho / \partial t)(\lambda_0, t) \to 0$ as $t \to T_{\lambda_0}$. Thus one strategy for finding λ_0 is to keep track, as t progresses, of a value L of λ for which $(\partial \rho / \partial t)(L, t) = 0$. This defines a curve $L(t)$. If the surface $S_{L(t)}(t)$ tends toward a limit, this limit is the candidate self-similar solution.

2.3. The General Algorithm

We now give the details of the general method. In this more general context, we again select a one-parameter family of initial surfaces $S_\lambda(0)$, the

level sets of some function $\varphi(x, 0)$. We then consider (conceptually) the two-parameter family of surfaces $S_\lambda(t)$, with $t \in [0, T_\lambda)$, and pick some function $\rho(\lambda, t)$ depending on the shape of $S_\lambda(t)$, to replace the ratio m_2/m_1 of Figure 2.

Recall that the level set formulation for curvature flow can be expressed as

$$\varphi_t = H_\varphi \|\nabla \varphi\|. \qquad (2.1)$$

We define a new function ψ as

$$\psi(x, t) = \frac{\varphi(\sigma(t)x, t)}{\sigma^2(t)} - L(t),$$

where $\sigma(t)$ is a stretching function and $L(t)$ is a level set switching function, both defined below. Differentiating this equation with respect to t and combining with (2.1) produces a new partial differential equation for ψ:

$$\psi_t = \frac{\sigma'(t)}{\sigma(t)} \left(x \cdot \nabla \psi - 2(\psi + L(t)) \right) + H_\psi \|\nabla \psi\| - L'(t) \qquad (2.2)$$

Here H_ψ is the mean curvature of the level surface of ψ that goes through (x, t).

The functions $\sigma(t)$ and $L(t)$ are determined dynamically. We choose $\sigma(t)$ so that the zero set of ψ has constant volume for all t. If we assume the interior of a surface is given by $\varphi(x, t) < 0$, and let

$$V(t) = \text{Vol}(\varphi(\cdot, t)^{-1}(0)) = \int_{\{x : \varphi(x, t) \le 0\}} dV,$$

we get

$$\sigma(t) = \left(\frac{V(t)}{V(0)} \right)^{1/3}$$

so that

$$\frac{\sigma'(t)}{\sigma(t)} = \frac{V'(t)}{3V(t)}$$

The functional $V'(t)/3V(t)$ is independent of scale, so we can evaluate it using ψ instead of φ. We approximate it numerically by assuming $\bar\varphi(x, t) = \psi(x, t)$ and then letting $\bar\varphi(x, t)$ flow by mean curvature alone (i.e., with σ kept fixed) to $\bar\varphi(x, t + \Delta t)$. By looking at the change of volume from this flow, we can compute $V'(t)/3V(t)$. This approximation

is convenient because it is easy to separate the curvature flow part of the evolution for ψ from the stretching and level switching part, as we will show.

The level function $L(t)$ is defined by the equation

$$\frac{\partial \rho}{\partial t}(L(t), t) = 0.$$

This is the $L(t)$ discussed at the end of Section 2.2.

We compute $\psi(x, t)$ numerically in a three step explicit scheme. The three steps are summarized as follows, where $\psi_n := \psi(x_{ijk}, t_n)$ and $\Delta t = t_{n+1} - t_n$:

- Set $\psi_{n+1} \leftarrow \psi_n + \|\nabla \psi_n\| H(\psi_n) \Delta t$.
- Set $V_{n+1} \leftarrow \text{Vol}\,\psi_{n+1}^{-1}(0)$ and $V_n \leftarrow \text{Vol}\,\psi_n^{-1}(0)$. Find L_{n+1} such that ρ has the same value for the L_{n+1}-level surfaces of ψ_n and ψ_{n+1}.
- Correct ψ_{n+1} by adding

$$\frac{V_{n+1} - V_n}{3V_n}(x \cdot \nabla \psi_n - 2(\psi_n + L_n)) - (L_{n+1} - L_n).$$

The first step is identical to the standard explicit numerical implementation of (2.1). This is where the curvature flow terms appear. In the second step, $\sigma(t)$ and $L(t)$ are determined according to information obtained in the first step. The third step makes the corrections to ψ needed to take into account stretching and level set shifting. Note that combining the first and third steps results in a straightforward explicit discretization of (2.2).

In all cases, we use central differencing to compute spatial derivatives, except for the term $x \cdot \nabla \psi_n$ where we use upwind differencing:

$$\begin{aligned} x \cdot \nabla \psi_n = &\max(0, x_1)D^1_- \psi_n + \min(0, x_1)D^1_+ \psi_n \\ &+ \max(0, x_2)D^2_- \psi_n + \min(0, x_2)D^2_+ \psi_n \\ &+ \max(0, x_3)D^3_- \psi_n + \min(0, x_3)D^3_+ \psi_n, \end{aligned}$$

where $D^1_\pm \psi_n = \pm(\psi(x_{(i\pm 1)jk}, t_n) - \psi(x_{ijk}, t_n))/\Delta x$ and so on. This follows the discretization used in [Osher and Sethian 1988].

If we apply this algorithm to the same initial conditions that produced Figure 4, the trajectories are transformed to those in Figure 5. The dashed line represents the zero set of ψ which will be our computed self-similar surface as t approaches T_{λ_0}.
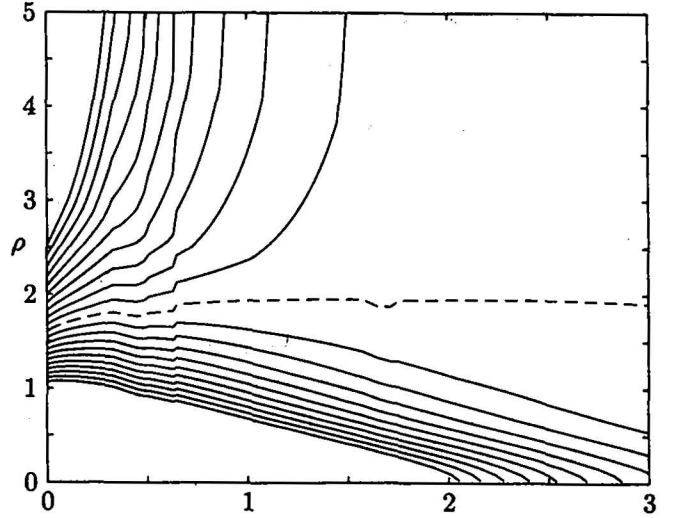

FIGURE 5. Trajectories of the level sets of ψ for the torus example, computed using the algorithm of Section 2.3 (compare Figure 4).

We conclude this section with two refinements to the algorithm just described.

2.4. Delay of Level Switching

Recall that $(\partial \rho/\partial t)(\lambda_0, t) \to 0$ as $t \to T_{\lambda_0}$; but this is expected only in a neighborhood of T_{λ_0}. In practice, the value of λ that makes $(\partial \rho/\partial t)(\lambda, 0)$ vanish may be quite far from λ_0, causing numerical problems for small t. For that reason, we make a preliminary estimate of λ_0, say l_0, using bisection, and replace the updating of $L(t)$ in the second step of the algorithm by:

- Find l such that ρ has the same value for the L_{n+1}-level surfaces of ψ_n and ψ_{n+1}. If $|L_n - l| < \varepsilon$, set $L_{n+1} \leftarrow l$; otherwise set $L_{n+1} \leftarrow l_0$.

This amendment delays the traversing of level sets until t is in a neighborhood of T_{λ_0}. We can see why this is a necessary precaution for small t by looking at Figure 4. The function $\rho(L(t), t)$, which is not shown but is sandwiched between those trajectories going to $+\infty$ and those going to 0, may not have a zero slope until long after $t = 0$. For some computations, this can lead the function $L(t)$ too far astray.

2.5. Time Scale and Reinitialization

It is worth noting that the equation of motion used here differs from the equations used by Huisken and others. In our equations we have not used rescaling in time to prevent singularity in finite time. This is for two reasons: we do not have a means of accurately computing the time of singularity for a given surface, and we must complete the computation in finite time.

This also means that at the time of singularity T, the computation must go unstable. We cannot compute all the way up to time T, but must stop short. We find that finer grids preserve stability longer than coarser ones, but the length of stability is also dependent upon the surface we are computing.

To compensate for this shortcoming, we periodically use reinitialization of the level set function ψ. When the calculation is approaching the time of singularity, we stop the computation and restart using the current zero set Z as the initial surface. The function ψ is then computed using the signed distance function from Z. The gain from reinitialization decreases rapidly with each use, so a typical computation will use as few as one reinitialization and no more than ten.

3. TESTS FOR SELF-SIMILARITY

Figure 6 compares cross-sections for the exact self-similar torus [Angenent 1992] and for an approximate one computed using our algorithm. The graph shows good agreement. For cases where an exact solution is not known, we will use two other tests for self-similarity. Applying these tests to the approximate torus solution gives a benchmark for comparison.

We start with a simple condition easily shown to be sufficient for self-similarity. We follow the argument presented in [Huisken 1991]. Suppose that Γ_0 is a two-manifold such that
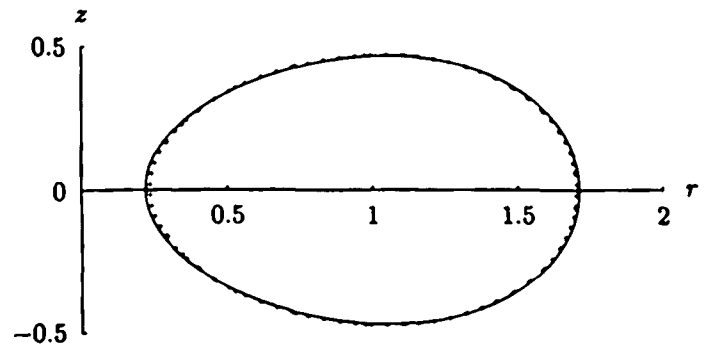
$$H(x) = \frac{1}{2T} x \cdot n \qquad (3.1)$$

FIGURE 6. Experimental (dots) and theoretical (curve) cross-sections for self-similar torus.

for each point $x \in \Gamma_0$, where n is the unit normal to Γ_0 at x, and T is some constant. Define

$$\Gamma_t = \frac{\sqrt{2(T-t)}}{\sqrt{2T}} \Gamma_0.$$

Then

$$\left(\frac{d}{dt} \Gamma_t \right)^\perp = \frac{\sqrt{2T}}{\sqrt{2(T-t)}} H_0 \cdot n = -Hn,$$

so that the family Γ_t represents a trajectory of the mean curvature flow. This shows that Γ_0 is a self-similar solution to the flow. T is the time to singularity for Γ_0.

This suggests the following test for self-similarity under the flow. We plot $x \cdot n$ versus H for points sampled evenly on the surface of interest. If the surface is self-similar, the points lie on a straight line, with slope $2T$. For an approximately self-similar surface S, we estimate the goodness of the fit by least squares: the estimated slope is

$$C = \frac{\sum_{i=1}^{N} x_i \cdot n_i}{\sum_{i=1}^{N} H_i},$$

and the (scale-invariant) error estimate is

$$E = \frac{1}{N} \sqrt{ \sum_{i=1}^{N} \left(H_i \sqrt{C} - \frac{1}{\sqrt{C}} x_i \cdot n_i \right)^2 }$$

For a self-similar torus computed on a rectangular grid of dimensions $120 \times 120 \times 60$, the computed
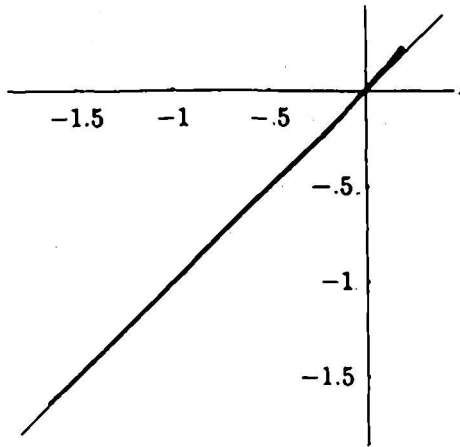
FIGURE 7.   Plot of $\frac{1}{\sqrt{C}} x \cdot n$ versus $\sqrt{C} H_i$ for torus.

error is $E = 0.007596$ (Figure 7). We consider that a surface is near self-similarity if E is of this order of magnitude.

Surfaces that fail this test tend to show points not tending towards collinearity and there is no improvement with time step or grid refinement (see Figure 24, for example).

Another test, applicable to compact surfaces, is to take the computed solution and evolve it according to the usual mean curvature flow. A self-similar solution should retain its shape for a considerable time as it shrinks.

4. EXPERIMENTAL RESULTS

We now turn to several experiments made with the algorithm of Section 2.3. For each one we describe the ratio function $\rho(\lambda, t)$ and the initial level sets, which will always be defined as equidistant sets from a certain initial surface. Most of the resulting surfaces appear to be self-similar under mean curvature flow; we show pictures of the surface and the results from the tests just discussed.

4.1. The Cube

Figure 9 shows a surface of genus five that we call the cube. It is obtained by applying the algorithm to the following data. For the initial zero level set $S_0(0)$ we take the boundary of a ball with three

cylindrical holes drilled along the coordinate axes (Figure 8 and Figure 10, left). As already mentioned, the remaining level sets $S_\lambda(0)$ are equidistant sets to $S_0(0)$.
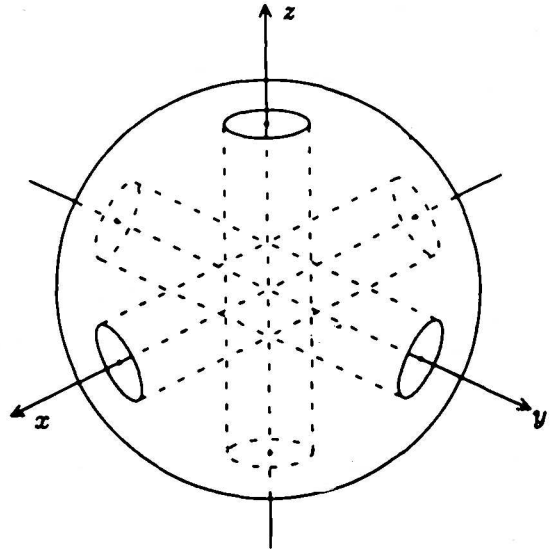
FIGURE 8.   Initial surface from which the cube evolves.

For ρ we take the ratio between the distance from the origin to the furthest point of the surface along the line $x = y = z$ and the distance from the x-axis to the point on the surface nearest the x-axis. Note that, for large ρ, the holes along the coordinate axes collapse. For small ρ, they expand outward and eventually join together, leaving eight balls.

The solution shown in Figure 9 appears to be a good approximation to a surface self-similar under the flow. The fit with the criterion (3.1) is good, as seen in Figure 11; the computed error is $E = 0.01869$. Moreover the surface retains its shape well under the usual mean curvature flow (Figure 12).

4.2 The Octahedron

The success of the previous computation leads to the conjecture that every regular polyhedron with holes will produce a corresponding self-similar solution for mean curvature flow. Figure 13 shows the octahedron, based on this idea. Again we begin
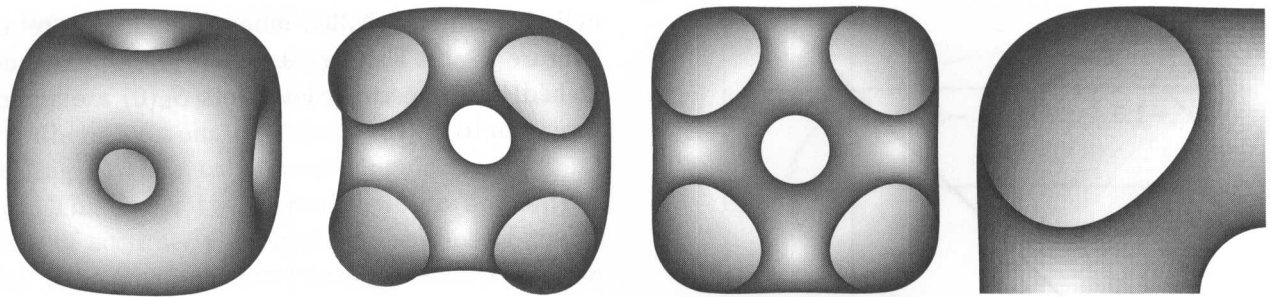
FIGURE 9.   Views of the self-similar cube (left), one-half of it (middle), and one octant (right).
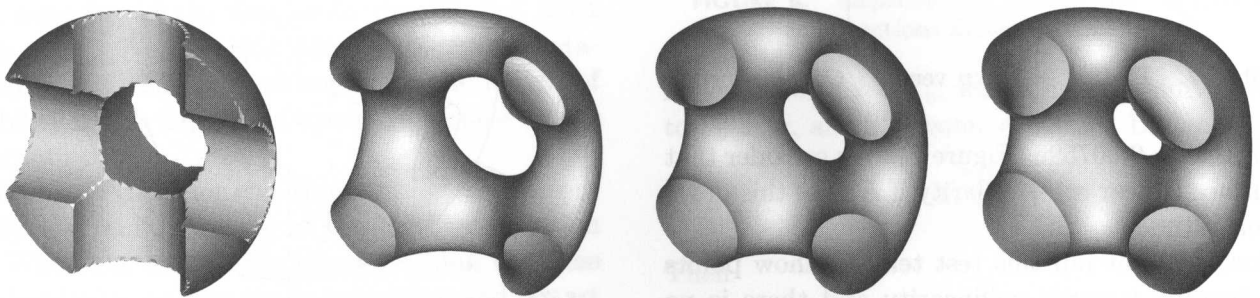

FIGURE 10.   Evolution toward the cube on a $60 \times 60 \times 60$ grid (for clarity, half the surface has been removed). Initially, level set switching is turned off (Section 2.4), so the holes tend to expand and break the connecting arms. After level set switching is activated, the holes begin shrinking again and the surface converges towards the final solution.
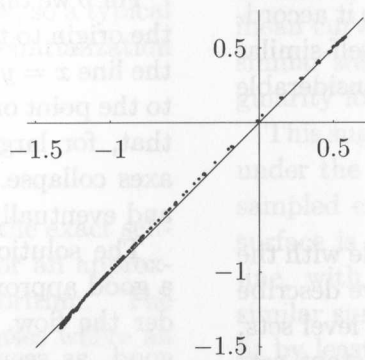

FIGURE 11.   Plot of $\dfrac{1}{\sqrt{C}}\, x \cdot n$ versus $H\sqrt{C}$ for the cube.
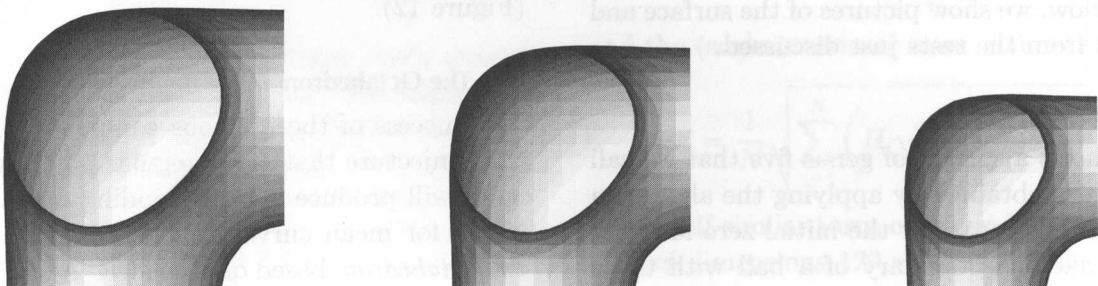
FIGURE 12.   Further evolution of the cube under mean curvature flow.
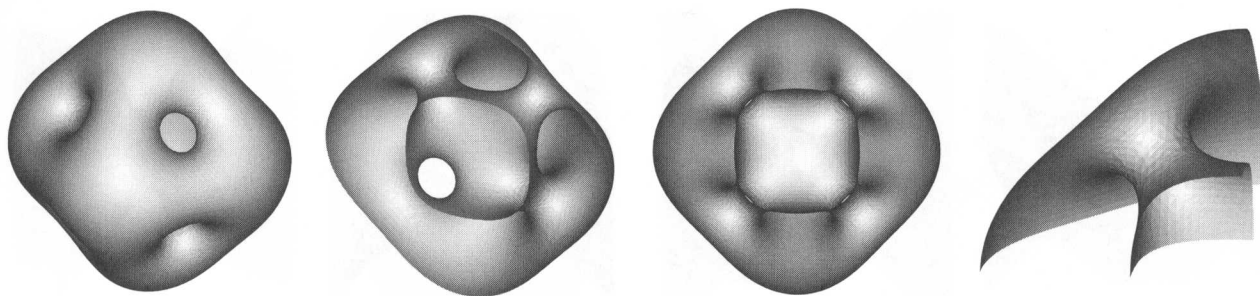
FIGURE 13. Views of the self-similar octahedron (left), half of it cut along a vertical plane (middle), and an octant (right). The computation was done on a $80 \times 80 \times 80$ grid. See also Figure 14.
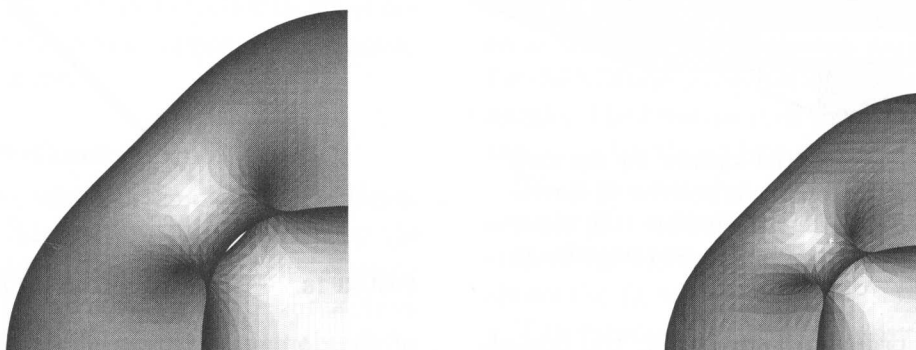
FIGURE 14. Further evolution of the octahedron under mean curvature flow.

with a sphere, this time with holes drilled diagonally along the vectors $(\pm 1, \pm 1, \pm 1)$. The rest of the construction is as for the cube. This surface has genus seven.

Again, we seem to get a good approximation to a self-similar surface. Figure 14 shows how the computed surface preserves its shape when it evolves under mean curvature. The fit with (3.1) is shown in Figure 15; the computed error is $E = 0.0197$.
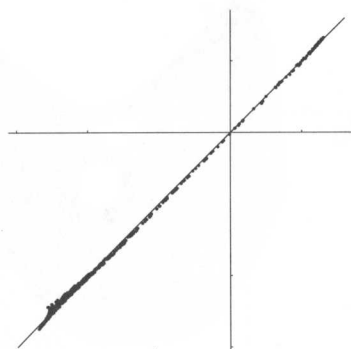
FIGURE 15. Plot of $\dfrac{1}{\sqrt{C}}\, x \cdot n$ versus $H\sqrt{C}$ for the octahedron.

4.3. The Saddle

The next example (Figure 16), called the *saddle*, arises from a suggestion by Matt Grayson and Tom Ilmanen. Topologically, it is a punctured torus, with eight-fold symmetry about the origin (reflections in the xz- and yz-planes, and interchange of x and y with simultaneous reflection in the xy-plane).

The initial surface consists of the xy-plane interrupted by two crossing tubes at the origin, as shown in Figure 17. As before, ψ is the distance function. The symmetry of this surface makes it unnecessary to use a ratio function: we expect the zero set to always be the correct level set.

Another difference from the algorithm of Section 2.3 is that here the volume on either side is the same regardless of how thin the handle gets. For this reason we used the cross-sectional area of one handle raised to the power $\frac{3}{2}$ in order to simulate a constant volume property.
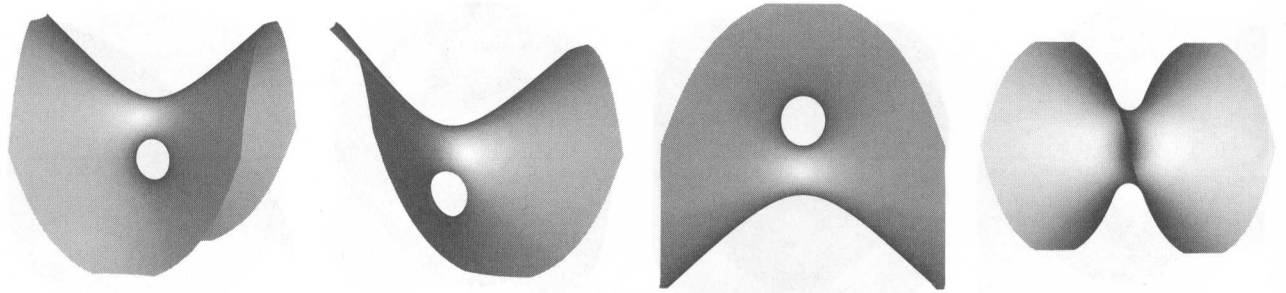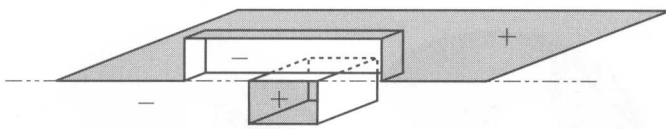
FIGURE 16. Views of the self-similar saddle.

FIGURE 17. Half the initial surface for the saddle. The distance function φ is positive in the region facing the gray side of the surface (the upper half-space and the lower tunnel), and negative in the complementary region.

FIGURE 18. Plot of $\dfrac{1}{\sqrt{C}}\, x \cdot n$ versus $H\sqrt{C}$ for the saddle.

The original surface is unbounded; the boundary conditions at the edges of the computational domain are taken to be upwind. This presents no problems, as the stretching function ensures that the upwind direction is always toward the origin (the surface is always expanding outward). The evolution is shown in Figure 19.

The tests indicate that this surface is close to self-similar (Figure 18); the computed error is $E = 0.005848$ (excluding the points on the boundary
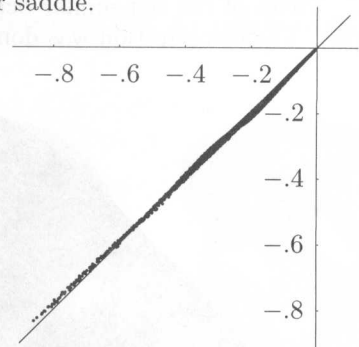
of the domain). Obviously, the tests can only be applied to that portion contained in the domain of computation. Whether there exists a complete surface that is self-similar cannot be demonstrated with this algorithm, but we can see that asymptotically this surface behaves as we would expect. If we look at the equation $H = (2T)^{-1} x \cdot n$, with T fixed, we see that as $x \to +\infty$ a solution may have $H \to 0$ while $x \cdot n \to 0$. This means that locally the surface gets flatter as it heads towards
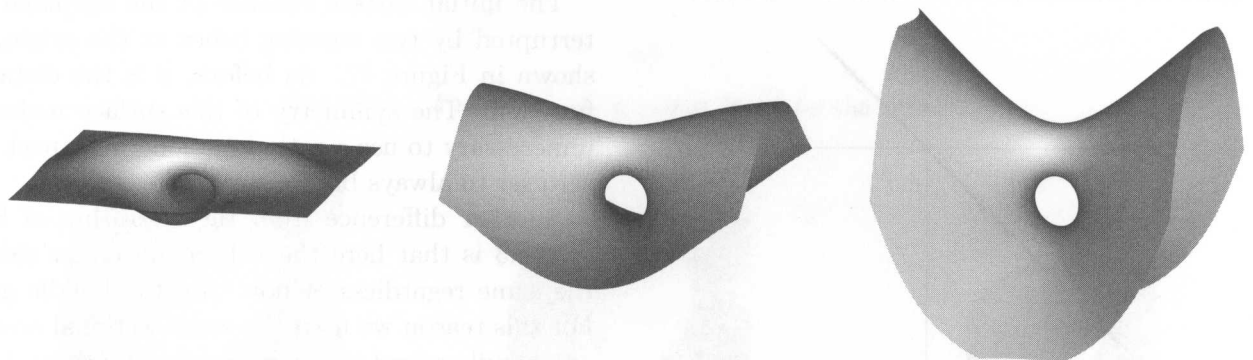

FIGURE 19. Evolution of the saddle on a $100 \times 100 \times 100$ grid. The two handles in the center expand outward and the holes in the plane tilt back to form the final surface.
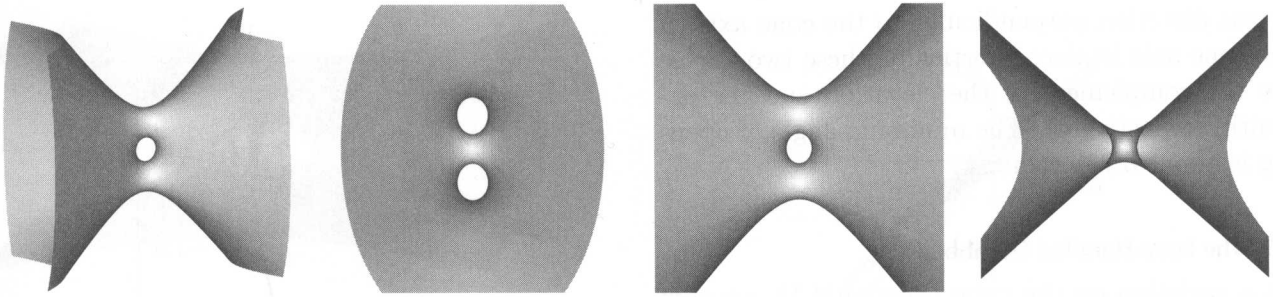
FIGURE 20.   Views of the self-similar two-handled cone. The computation took place on a $100 \times 100 \times 100$ grid.

infinity, while the surface normal tends to become orthogonal to x. We see this behavior in all of our unbounded examples as they appear to asymptotically approach a cone.

4.4. The Two-Handled Cone

The next example, which is topologically a twice-punctured torus (Figure 20), was inspired by the success of the saddle. The initial surface consists of two horizontal planes combined with three crossing tubes (Figure 21). The function ψ is again distance, and ρ is the ratio between the cross-sectional areas of the top and middle handles. For ρ large,
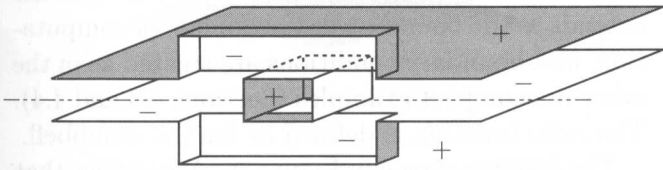

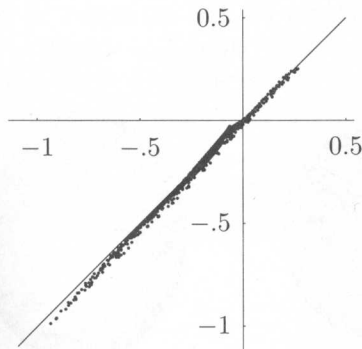**FIGURE 21.**   Half the initial surface for the cone with two handles.

the middle hole gets thinner and collapses, and for ρ small, the top and bottom handles collapse. The cross-sectional area of the top handle was also used for the volume computation, as in the previous example. The treatment of the boundary conditions, too, is as for the saddle.

The surface is close to self-similar; the computed error is $E = 0.01983$, again excluding points of the surface on the boundary of the domain. Figure 22 shows the fit with equation (3.1).

This example, if it can be proved to exist, may be a candidate for an initial smooth surface that develops an interior. The asymptotic behavior seems to be that of a cone, so that at the time of singularity the surface should become a cone. Preliminary research by Ilmanen and Angenent indicates that a cone with a large enough angle of opening will form an interior according to the theory of weak solutions. However, the value of the critical angle of opening is yet to be determined. In the event that such an angle is found, we show in Figure 23 sampled points giving the angle of opening in radians
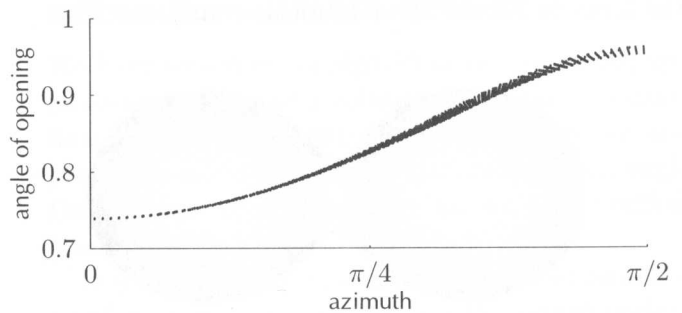

FIGURE 22.   Plot of $\dfrac{1}{\sqrt{C}} x \cdot n$ versus $H\sqrt{C}$ for the two-handled cone.

FIGURE 23.   Angle of opening versus azimuth for the two-handled cone.

versus direction perpendicular to the cone axis (if the cone axis is placed vertically, these two angles are the complement of the elevation and the azimuth, respectively). The minimum angle of opening is about 0.739 radians.

4.5. The Four-Handled Dumbbell

As a variation on the cube (Section 4.1), we now take an initial surface like that of Figure 8, but instead of three holes through the ball we drill only two, along the x- and y-axes. For ρ we take the ratio between the diameter of a component of the section of the surface by the xy-plane, and the distance from the x-axis to the point on the surface nearest to the x-axis. (The exact definition of ρ does not matter much; we tried other definitions, with essentially the same results.)

As it turns out, the algorithm here does not lead to a self-similar solution. A typical "final" surface is shown in Figure 24. One sees that, no matter how fine the grid (here $60 \times 60 \times 120$), the computation becomes meaningless beyond a certain point because of the growing difference in scale between the lobes and the handles, which squeezes out all detail from the central region. The computed error for this surface is $E = 0.584$ and the fit with (3.1), shown in Figure 25, is very poor.

In retrospect, this makes sense: for a self-similar surface, big regions far from the origin ($\|x\|$ large) must nearly be tangent to the direction of x, since $x \cdot n$ is proportional to H and we cannot expect H to be large over big regions. The outer halves of the lobes in Figure 24 violate this condition. This
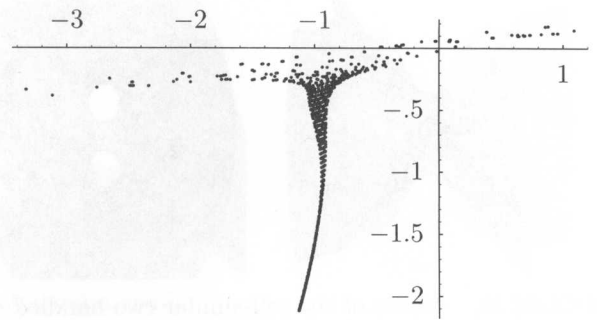

FIGURE 25. Plot of $\dfrac{1}{\sqrt{C}} x \cdot n$ versus $H\sqrt{C}$ for the surface of Figure 24.

suggests that we should focus around the origin, replacing the two lobes by a cone. Indeed, one can discern a straight-line pattern in Figure 25 among those points with $x \cdot n$ near zero; roughly speaking, these data points correspond to sample points on the surface near the origin.

4.6. The Four-Handled Cone

To test this hypothesis, we choose as an initial surface the boundary of a vertical cylinder (instead of a sphere, as in the previous section) with two holes drilled along the x- and y-axes. The cylinder extends to the boundary of the domain of computation, and boundary conditions are treated as in the other noncompact examples (Sections 4.3 and 4.4). The ratio function is defined as for the dumbbell.

The result is shown in Figure 26. We believe that this surface does approximate a self-similar one, in spite of the somewhat greater deviation from collinearity than for the examples in Sections 4.1 to 4.4 (Figure 27). Here $E = .0505$.
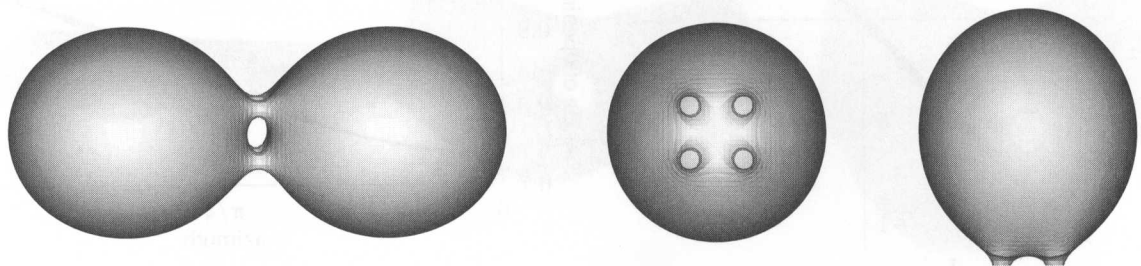

FIGURE 24. Computed "solution" for the dumbbell. This surface is not self-similar under mean curvature flow. (The image on the left has been turned, so the z-axis is horizontal.)
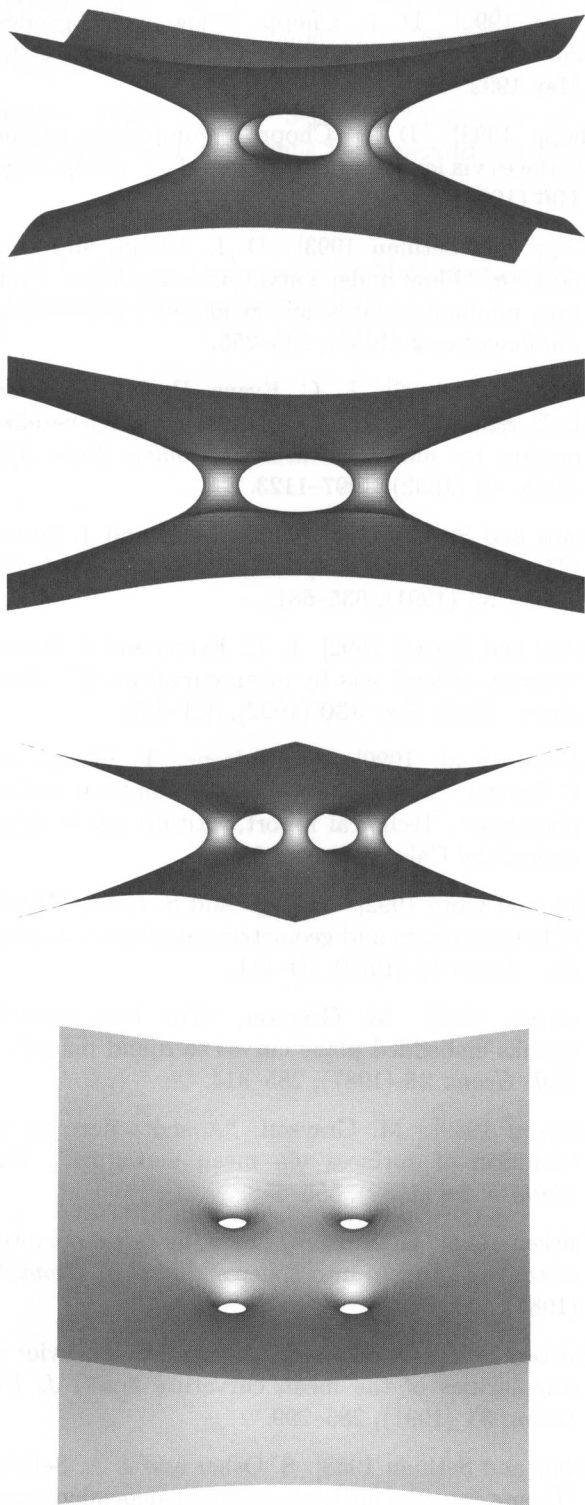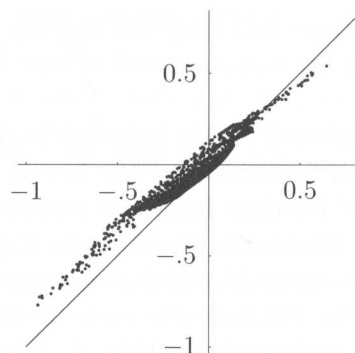
FIGURE 27. Plot of $\dfrac{1}{\sqrt{C}}\, x \cdot n$ versus $H\sqrt{C}$ for the four-handled cone.

Note that the angle of opening for the limiting cone of this surface is considerably larger than for the two-handled cone (Figures 26 and 28). The minimum angle of opening is about 1.2627 radians. This makes it an even likelier candidate for developing interior (see the discussion at the end of Section 4.4).
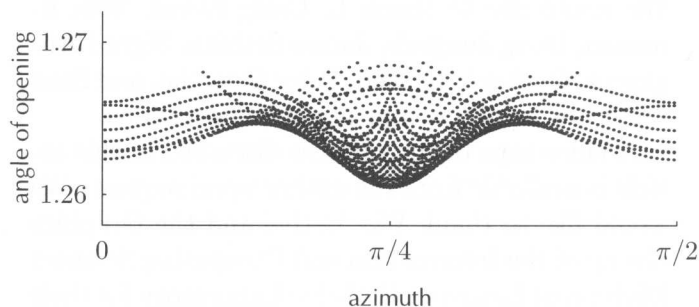

FIGURE 28. Angle of opening versus azimuth for the four-handled cone.

5. CONCLUSION AND FUTURE WORK

We have presented an algorithm for computing approximate self-similar solutions of mean curvature flow. We have computed what appear to be approximations to new self-similar surfaces, although the existence of such surfaces has not been verified theoretically.

In particular, the two-handled and four-handled cones may contribute substantially toward understanding mean curvature flow and the types of singularities that can occur from an initially smooth

FIGURE 26. The four-handled cone, computed on a $160 \times 160 \times 160$ grid.

surface. We hope that they will also aid in proving the existence (or nonexistence) of new self-similar solutions.

One shortcoming of this approach is the symmetry restriction for solutions. We intend to remove one degree of freedom from this restriction by increasing the dimension of the space $S_\lambda(0)$ to two, and thus the space U will have dimension three. In this case, we will have two ratio functions ρ_1, ρ_2 for selecting trajectories within U. The resulting formulation should have domain contained in $\mathbb{R}^4$. Higher-dimensional domains are probably impracticable with current technology.

In this higher dimension, we hope to find more self-similar solutions that are not possible with the current method. Two of our intended solutions will be semi-regular polyhedra and a trefoil knot.

Acknowledgments

REFERENCES

[Altshuler et al. 1993] S. Altshuler, S. B. Angenent and Y. Giga, "Mean curvature flow through singularities for surfaces of rotation" (preprint).

[Angenent 1992] S. Angenent, "Shrinking doughnuts", pp. 21–38 in *Nonlinear Diffusion Equations and Their Equilibrium States*, 3, (edited by N. G. Lloyd et al.), Birkhäuser, Boston, 1992.

[Chen et al. 1991] Y. Chen, Y. Giga and S. Goto, "Uniqueness and existence of viscosity solutions of generalized mean curvature flow equations", *J. Diff. Geom.* **33** (1991) 749–786.

[Chopp 1992] D. L. Chopp, "Flow under geodesic curvature", Technical Report CAM 92-23, UCLA, May 1992.

[Chopp 1993] D. L. Chopp, "Computing minimal surfaces via level set curvature flow", *J. Comp. Phys.*, **106** (1993), 77–91.

[Chopp and Sethian 1993] D. L. Chopp and J. A. Sethian, "Flow under curvature: singularity formation, minimal surfaces, and geodesics", *Experimental Mathematics* **2** (1993), 235–255.

[Evans et al. 1992] L. C. Evans, H. M. Soner, and P. E. Souganidis, "Phase transitions and generalized motion by mean curvature", *Comm. Pure Appl. Math.* **45** (1992), 1097–1123.

[Evans and Spruck 1991] L. C. Evans and J. Spruck, "Motion of level sets by mean curvature I", *J. Diff. Geom.* **33** (1991), 635–681.

[Evans and Spruck 1992] L. C. Evans and J. Spruck, "Motion of level sets by mean curvature II", *Trans. Amer. Math. Soc.* **330** (1992), 321–332.

[Falcone et al. 1990] M. Falcone, T. Giorgi, and P. Loretti, "Level sets of viscosity solutions and applications", Technical report, Istituto per le Applicazioni del Calcolo, Rome, 1990.

[Giga and Goto 1992] Y. Giga and S. Goto, "Motion of hypersurfaces and geometric equations", *J. Math. Soc. Japan* **44** (1992), 99–111.

[Grayson 1987] M. Grayson, "The heat equation shrinks embedded plane curves to round points", *J. Diff. Geom.* **26** (1987), 285–314.

[Grayson 1989] M. Grayson, "A short note on the evolution of surfaces via mean curvature", *Duke Math. J.* **58** (1989), 555–558.

[Huisken 1984] G. Huisken, "Flow by mean curvature of convex surfaces into spheres", *J. Diff. Geom.* **20** (1984), 237–266.

[Huisken 1991] G. Huisken, "Asymptotic behavior for singularities of the mean curvature flow", *J. Diff. Geom.* **31** (1991), 285–299.

[Osher and Sethian 1988] S. Osher and J. A. Sethian, "Fronts propagating with curvature-dependent speed: Algorithms based on Hamilton–Jacobi formulations", *J. Comp. Phys.* **79** (1988), 12–49.

[Sethian 1985]   J. A. Sethian, "Curvature and the evolution of fronts", *Comm. Math. Phys.* **101** (1985), 487–499.

[Sethian 1989]   J. A. Sethian, "A review of recent numerical algorithms for hypersurfaces moving with curvature-dependent speed", *J. Diff. Geom.* **31** (1989), 131–161.

[Sethian and Strain 1992]   J. A. Sethian and J. Strain, "Crystal growth and dendrite solidification", *J. Comp. Phys.* **98** (1992), 231–253.

David L. Chopp, Department of Mathematics, GN-50, University of Washington, Seattle, WA 98195 (chopp@math.washington.edu)